The role of fluid chemistry, pressure, and temperature on deformation microstructures in limestone

Shayna Quidas

GEOL 394

Advisors: Dr. Wen-lu Zhu and Harry Lisabeth

April 25, 2016

Table of Contents

Abstract

Interstitial pore fluids exert important controls on the mechanical and chemical processes that take place during rock deformation. Recent experiments show that the presence of pore fluid can significantly reduce the yield strength of Indiana limestone (Lisabeth and Zhu, 2015). I hypothesize that this reduction in yield strength results from enhanced twinning and dissolution, owing to the low critical resolved shear stress and relatively high solubility of calcite. Further, twinning and dissolution during deformation are sensitive to temperature and fluid chemistry. To test my hypothesis, I performed quantitative microstructural analysis on triaxially deformed Indiana Limestone samples. Linear densities of microcracks, mechanical twins, and indentations along grain boundaries are measured in samples deformed over a range of pressures (10-50 MPa), temperatures (23-75°C), and fluid chemistry conditions. Linear density was calculated by counting occurrences of features along lines oriented parallel and perpendicular to the direction of maximum principal stress, resulting in units of counts per mm. My results indicate that calcite twin density increases and microcrack linear density decreases with increasing pressure, which suggests a transition from brittle to plastic deformation. Fluid composition also influences the formation of microstructures: samples saturated with distilled water have a greater density of microcracks, calcite twins, and indentations compared to samples saturated with pore fluids that are in chemical equilibrium with the carbonate rock.

1. Introduction

Interstitial pore fluids are known to control the mechanical strength and compaction behaviors of rocks. Decreasing pore pressure $p_p$causes an increase in the effective stress σ_{eff}:

$$\sigma_{eff} = \sigma_T - p_p \quad (1)$$

where σ_T is the overburden. The effective stress law (e.g. Terzaghi, 1943) can explain the subsidence commonly associated with fluid pumping. For instance, between 1974 and 1985 the Ekofisk oil platform subsided roughly 4 meters due to a reduction in pore pressure in the chalk layer being pumped (Doornhof et al., 2006; Nagel 2001). This change in effective stress caused a considerable change Δt in the thickness of the chalk layer, seen in equation (2):

$$\Delta t = c \times h \times \Delta\sigma_{eff} \quad (2)$$

where c is compressibility of the rock, h is the original rock unit thickness, and $\Delta\sigma_{eff}$ is the change in effective stress.

As fluid was continuously pumped out, the effective stress continued to increase and thus the volumetric strain increased (i.e., compaction). At large changes in effective stress an elastic limit is reached. The elastic limit is the maximum stress a rock can withstand before permanent deformation occurs (Figure 1). Beyond the elastic limit, a small increase in effective stress can result in a large increase in volumetric strain (i.e., accelerated compaction), which is termed shear-enhanced compaction. The chalk reservoir rock at the Ekofisk field had reached its elastic limit and experienced an accelerated compaction.

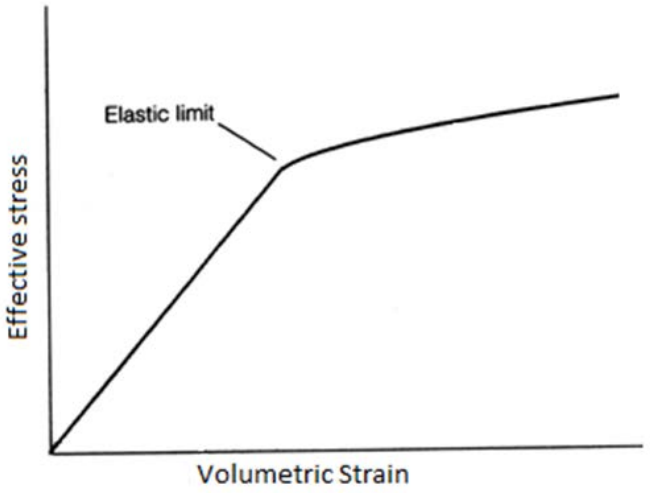

Figure 1: Relationship between effective stress and volumetric strain.

To stop the accelerated compaction, Phillips Petroleum, the company that owned the platform, began to inject seawater into the chalk layer in 1986. With the introduction of fluid, the pore pressure rose and the subsidence rate decreased to roughly 15 cm per year by 2002. However, compaction did not cease. Shortly after 2005 the subsidence rate once again began to rise, despite the re-establishment of pore pressure. The injected seawater was dissolving the chalk layer, causing deformation, and leading to further compaction (Doornhof et al., 2006; Nagel, 2001). The solubility of calcite in water may have a significant influence on deformation of chalk and other calcium carbonate

rocks. The coupling between both chemical and mechanical deformation processes that occur in the presence of fluids is not fully understood. A better understanding of the role fluid chemistry has on deformation is needed. This study focuses on the effect of fluid chemistry on deforming limestone, a calcium carbonate rock. Better understanding of the fluid-rock interactions, especially on how fluid chemistry affects the mechanical strength and deformation behaviors of porous sedimentary rocks, is essential in many energy and environmental applications, such as oil and gas exploration, waste water disposal, and mitigation of injection induced seismicity (Ellsworth, 2013).

2. Background

Limestone is a sedimentary rock consisting of calcite and aragonite ($CaCO_3$). Limestone is moderately porous and permeable, allowing the transmission of fluids within pore space, including water. Falling rainwater reacts with carbon dioxide in the atmosphere and soil. Carbon dioxide-charged water then can seep into the ground as groundwater. When acidic groundwater comes into contact with limestone, the CO_2-charged water dissolves the calcium carbonate, shown by the following chemical reaction;

$$CaCO_3 + H_2O + CO_2 \rightleftharpoons Ca^{2+} + 2HCO_3^- \quad (3)$$

Under mechanical loading, the reaction of carbon dioxide and water with calcium carbonate can be described as both a mechanical and chemical process. When a rock is deformed inelastically, different types of microstructures are produced. Typically, microcracking along with calcite twinning can occur when a carbonate rock is deformed at low-temperature. Chemically, due to the solubility of calcite in water, dissolution/precipitation processes may occur concurrently. This is different from deformation mechanisms observed in quartz-dominated sandstones saturated with water, where Hertzian fracturing and frictional sliding are the dominant deformation mechanisms (Menendez et al., 1996). The coupling between mechanical and chemical effects may exert significant control over the deformation mechanisms and microstructures in carbonate rocks.

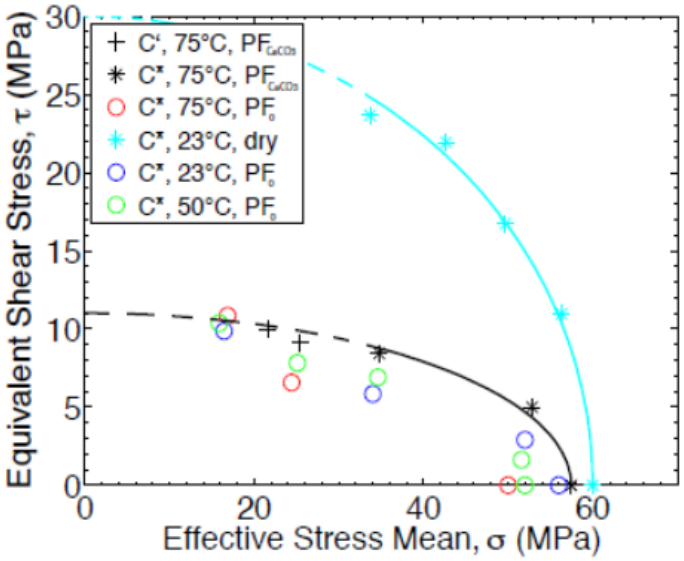

Figure 2: Yield strength of limestones deformed from Lisabeth and Zhu (2015). Open circles and black asterisks represent onset of shear-enhanced compaction for the given conditions. Black crosses represent the onset of dilatancy. PF_{CaCO3} refers to samples saturated in fluid that was allowed to reach equilibrium with the rock. PF_0 refers to samples saturated in distilled water that was not allowed to reach equilibrium with the rock.

A recent study by Lisabeth and Zhu (2015) examined the yield strength and deformation mechanisms of Indiana Limestone samples at a range of pressure, temperature, and fluid chemistry conditions. Their study concluded that pore fluid present in limestone can cause an up to 60% yield strength reduction compared to dry samples (Figure 2). The deformation microstructures present included pressure solution, microcracking, and calcite twinning (Lisabeth and Zhu, 2015). The preliminary results also show that deformation microstructures vary at different experimental conditions.

3. Deformation Microstructures

Microcracking occurs when local stress exceeds local strength. Microcracks can form at grain boundaries, within grains, or across grains (Simmons and Richter, 1976). Extensive microcracking leads to cataclasis, a type of brittle deformation commonly observed in fault zones. Pore fluid within a rock can reduce its strength via corrosion and thus cause microcracking at lower stress levels. During the triaxial deformation, shortening in a rock occurs parallel to the direction of maximum stress, σ_1, whereas lengthening occurs parallel to the direction of minimum stress, σ_3. Propagation of microcracks occurs perpendicular to the direction of minimum stress. Vajdova et al. (2010) show that in Tavel limestone (without pore fluid), microcracks are parallel to the maximum principal stress σ_1 when samples failed in the brittle faulting regime. However at higher pressures, microcracks did not have a preferred orientation in samples failed by cataclastic flow regime (Vajdova et al., 2012). Microcracks cause dilatancy, known as an increase in volume due to widening of microcracks. In porous rocks, whether a deforming rock exhibits dilatancy or compaction depends on initial porosity, confinements, and failure modes.

Three twin types can occur via different modes of formation: growth twins, transformation twins, and gliding twins. Here we will focus on gliding or deformation twins, the result of stress

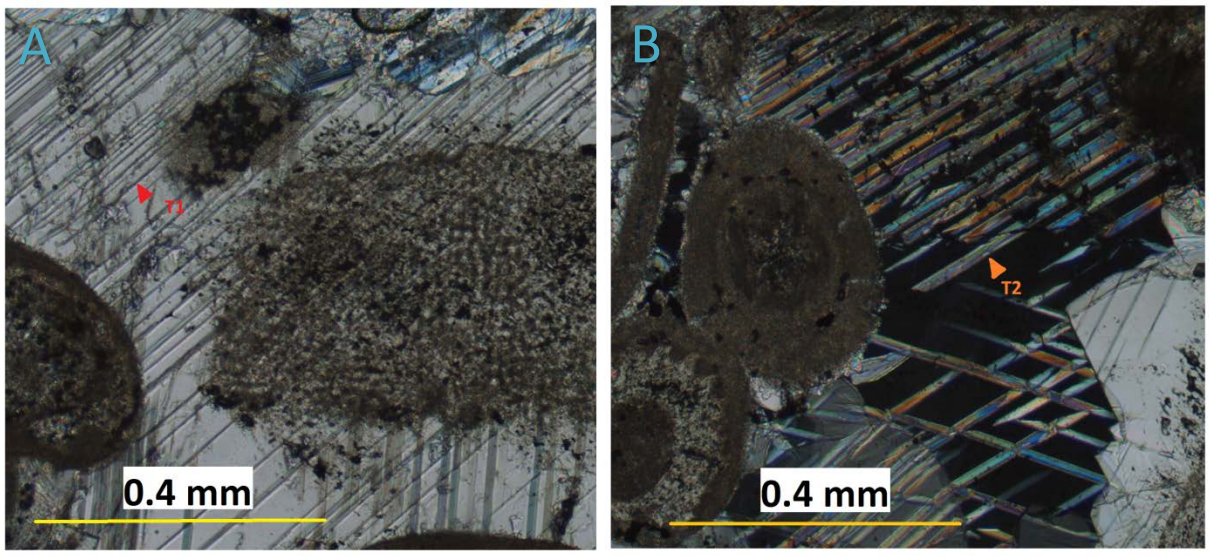

Figure 3: Type 1 and type 2 calcite twins. Type 1 are thin twins, less than a micron in width and type 2 are thick twins, between 1 to 10 microns in width. (A) Thin section IndLs3-8 with a red arrow pointing to a type 1 twin. (B) Thin section IndLs5-3 with an orange arrow pointing to a type 2 twin. Both images are taken at 10x under cross-polarized light.

applied to the crystal after formation. In calcite, twin gliding is often the dominant form of twinning. These twins are produced via shearing that causes kinks in the crystallographic structure. Repeating kinks within a crystal structure causes twin lamellae to form. The plane where kinks occur is called a twin plane and is optically visible under a microscope. Due to the crystallographic structure of calcite, its critical resolved shear stress is relatively low, thus low shear stresses can initiate mechanical twinning (Vajdova et al., 2004). Temperature also exerts control on calcite twins, changing the appearance of calcite twin lamellae. At temperatures below 170 °C twins are thin, generally less than a micron in width. With increasing temperature, calcite twin width also increases; above 200 °C thick twins 1 to 10 microns in width are dominate (Figure 3; Burkhard, 1993). Ferrill et al. (2004) expanded on this approach and quantified the relationship between calcite twin width and density. Ferrill et al. concluded that at temperatures below 170 °C twin strain is accommodated mostly by increasing the number of thin twins, and at temperatures above 200 °C twin strain is accommodated mostly by increasing the width of the twins. This study allows for calcite to be used as a low-temperature deformation geothermometer, but does not address how the introduction of pore fluids may or may not influence this geothermometer.

Pressure solution may also occur during deformation of carbonate rocks due to the relatively high solubility of calcite. Pressure solution is described by three steps: dissolution of grain material at high stress contacts, diffusion of material along grain boundaries and pores, and precipitation in areas of low stress on free pore walls (Rutter, 1983; Niemeijer et al., 2002; Zhang et al., 2011). At high stress grain boundary contacts, indentation of grains or sutured intergranular contacts occur as a result of the dissolution step of pressure solution (Figure 6; Rutter 1983). Previous studies have concluded that chemistry of the pore fluid in limestones does affect pressure solution and creep rate (Zhang and Spiers, 2005; Zhang et al., 2011) along with temperature and pressure (Niemeijer et al., 2002). Grain size also affects pressure solution; strain rate is inversely proportional to grain size (Niemeijer et al., 2002; Zhang and Spiers, 2005).

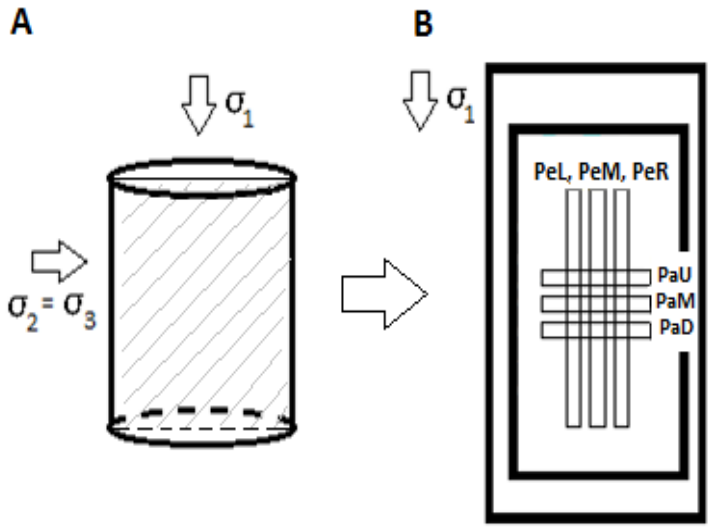

Figure 4: (A) Schematic diagram of deformation of the cylindrical Indiana Limestone samples. Relationship between the maximum (σ_1), intermediate (σ_2), and minimum (σ_3) principal stress directions are indicated. For samples deformed hydrostatically all principal stressors are equal. The gray shaded area indicates the area of the thin section created from the deformed cylinder. (B) Schematic of thin section analysis by linear density analysis. Photomicrographs were taken along the rectangular areas named PeL, PeM, PeR, PaU, PaM, and PaD. Pe indicates photomicrographs taken perpendicular to σ_1 and Pa indicates photomicrographs taken parallel to σ_1. Photomicrographs were taken along four additional rectangular areas, PeRR, PeLL, PaUU, and PaDD, but are not shown.

An understanding of how pressure and temperature affect deformation microstructures in limestone is

important, but incomplete without taking into account interstitial fluid. Many rocks in the field are partially saturated with fluid, thus fluid chemistry should be addressed to relate lab-deformed rocks to rocks deformed by natural processes. Chemo-thermo-mechanical coupling may greatly influence deformation microstructures and should be closer examined.

4. Hypotheses

My hypotheses are:

(1) Fluid chemistry does affect the deformation microstructures in limestones.

(2) Fluid chemistry will affect the intensity of twinning.

(3) Coupling of mechanical and chemical loads will enhance dissolution.

5. Objective and Methods

This study addresses how fluid chemistry, temperature, and pressure affect deformation microstructures in limestones. Deformed Indiana Limestone samples (Lisabeth and Zhu, 2015) were obtained for this study. Indiana Limestone is a fairly homogenous calcarenite limestone with roughly 16% porosity. The rock is 98% calcite and ~1% oxides and trace clay minerals. Allochemical clasts and sparry calcite compose the rock, with microcrystalline micrite often coating the allochemical clasts. Samples were cored perpendicular to bedding and ground into cylinders to be used in triaxial deformation experiments. Experiments were performed over a range of temperatures, effective confining pressures, and fluid chemistry conditions: 23-75 °C, 10-50 MPa and hydrostatically, and with two types of fluid (Table 1). Experiments used both distilled water that was not allowed to reach equilibrium with the rock (PF_0) and distilled water that was allowed to reach equilibrium with the rock (PF_{CaCO_3}). In the triaxial deformation experiments $\sigma_1 > \sigma_2 = \sigma_3$; during hydrostatic deformation experiments $\sigma_1 = \sigma_2 = \sigma_3$ (Figure 4A). After deformation experiments were completed samples were prepared for thin section analysis. Samples were permeated with epoxy and then bisected parallel to σ_1 to make double-polished thin sections (Lisabeth and Zhu, 2015).

Sample Name	Fluid	Temperature °C	Pressure MPa
IndLs3-8	PF_0	75	10
IndLs3-17	PF_0	75	50
IndLs5-3	PF_{CaCO_3}	75	10
IndLs5-8	PF_{CaCO_3}	75	50

Table 1: Deformation conditions for each thin section from Lisabeth and Zhu (2015). PF_0 indicates distilled water that was not allowed to reach equilibrium with the rock, PF_{CaCO_3} indicates fluid was allowed to reach equilibrium with the rock.

This study quantitatively analyzes microstructures within these thin sections with a Nikon Eclipse LV100n POL petrographic microscope. All photos have been taken with a MicroPublisher 5.0 RTV camera.

Microstructural features analyzed include: microcrack density, indentation along grain boundary density, and calcite twin density. Indentation along grain boundaries will be used here to quantify the degree of dissolution (Rutter, 1983).

5.1 Microcrack Analysis

Density of the microcracks was calculated by linear density analysis, a previously established method (Menendez et al., 1996; Wu et al., 2000; Cilona et al., 2010; Vajdova et al., 2010). A series of photomicrographs at a magnification of 10x was taken along lines both perpendicular and parallel to σ_1 to assess the anisotropy of microcracking within the sample. The maximum grain size for Indiana Limestone is 1 mm, and the lines used for analysis were spaced 3 mm apart (Frew et al., 2010). If microcrack density is greater perpendicular to σ_1 than parallel to σ_1 microcracks have developed preferentially to the maximum stress axis, and the degree of stress-induced anisotropy may be calculated (Menendez et al., 1996). A line was drawn down the center of the photomicrographs; microcracks intercepted by this line were counted as incidents. The length of the line was measured, and allowed the microcrack count per mm to be calculated. To reduce error and bias ten lines were taken, five perpendicular to σ_1 and five parallel to σ_1 (Figure 4B). The average microcrack density was calculated for the two orientations of lines for each thin section. Uncertainty was quantified by calculating the standard deviation of the average,

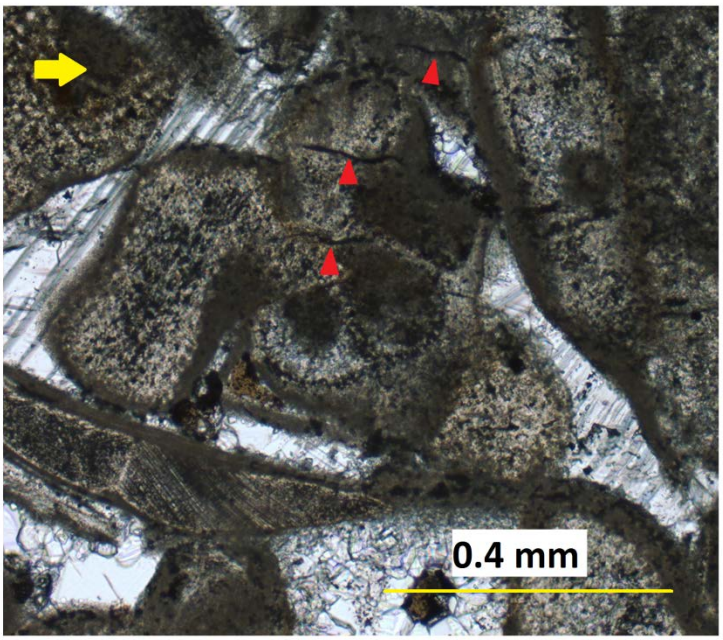

Figure 5: Thin section IndLs3-8 at 10x under PPL. Red arrows point to microcracks forming across an allochemical clast. The yellow arrow is oriented parallel to σ_1 .

$$\sigma = \sqrt{\frac{1}{N-1}\sum_{i=1}^{n}(x_i - \bar{x})^2} \tag{3}$$

where N is the total number of lines, $\bar{x}$ is the average density per mm, and x_i is density per mm.

Uncertainty in measuring the length of the point-count line is currently 0.05 mm, as 0.1 mm is the smallest measuring increment currently available. In cases where an uncertainty of 0.05 mm would not affect the density of the microcracks, uncertainty in the length of the line can be approximated to 0.

5.2 Calcite Twin Analysis

Two types of calcite twins are present in the thin sections, Type 1 and Type 2. The temperature range for the triaxial deformation experiments did not exceed 75 °Celsius, so all Type 2 twins present in the samples can be assumed to have formed before deformation experiments were performed (Figure 3; Burkhard 1993). The density of calcite grains exhibiting twins in the undeformed sample was very low, so the majority of twins in the deformed samples formed during deformation experiments. For twinned calcite grains linear density analysis was used; a grain with one set of twins counted as 1, and a grain with two sets of twins counted as 2. Twin formation generally reduces stress via dislocation. Forming a second set of twins requires additional stress, and so grains with two sets of twins count as 2. Uncertainty in the average density was calculated with equation (3).

Some microcracks, indentations, and calcite twins may have formed before deformation experiments and so an undeformed thin section of Indian Limestone was analyzed to find the average density of microcracks, indentations, and calcite grains exhibiting twins before experiments were performed. These data were used to calculate the actual density of the microstructural features after experiments were performed. Uncertainties in these data were calculated with equation (3).

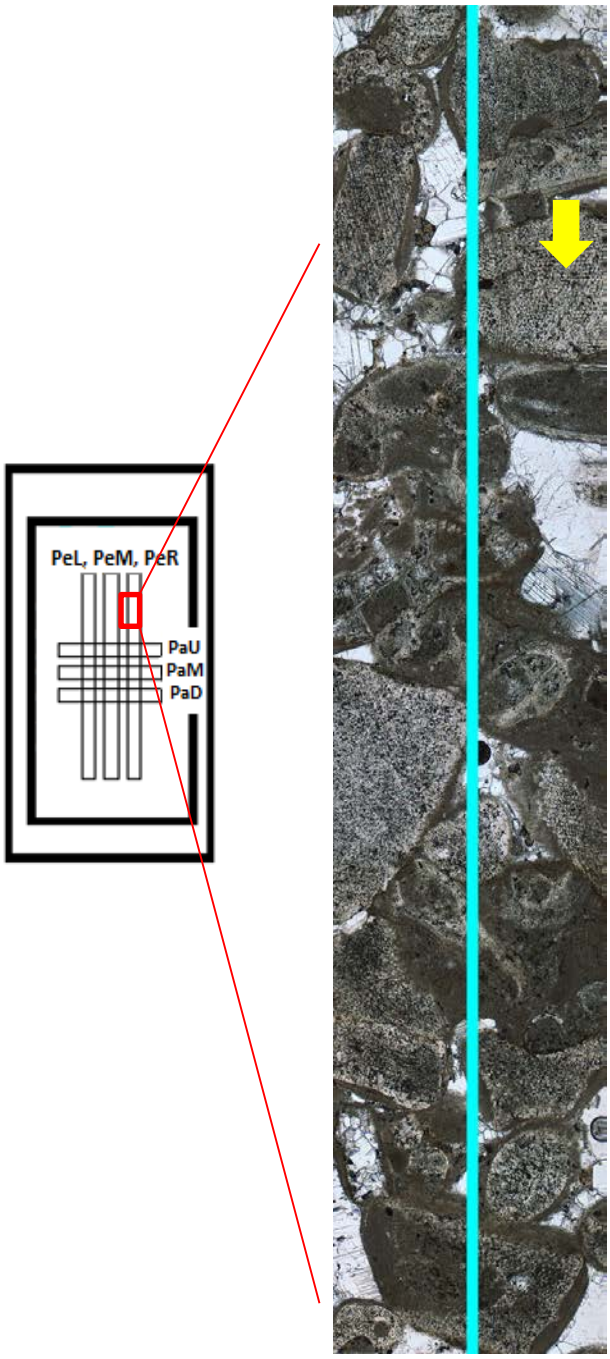

Figure 6: Example of a partial strip of photomicrographs used in linear density analysis. Incidents that occur touching the blue line are counted and then divided by the total length of the line to get counts per mm. The yellow arrow indicates the direction of σ_1.

5.3 Indentation Analysis

Dissolution was quantified by counting incidents of indentation or sutured grain-boundary. Two types of indentation were quantified, I1 and I2. Grains that touch along a shared grain-boundary and that are not obviously indented are I1-type indentations (Figure 6A). Grains that do indent onto another or are sutured along their grain-boundary are I2-type indentations (Figure 6B). I2-type indentations accommodate the most strain. As with microcracking, linear density analysis was used to count the incidents of indentations along grain boundaries. In this paper, indentation density refers to the density of indentation features along grain boundaries, not the actual density of dissolution. If I2-type

indentations are more abundant parallel to σ_1 than perpendicular, then dissolution occurred preferentially parallel to the maximum principal stress axis. This conclusion may be further strengthened if I2-type indentations parallel to σ_1 are more abundant than I1-type indentations.

An average was calculated for incidents along lines parallel to σ_1 and perpendicular to σ_1. Uncertainty in the average will come from equation (3).

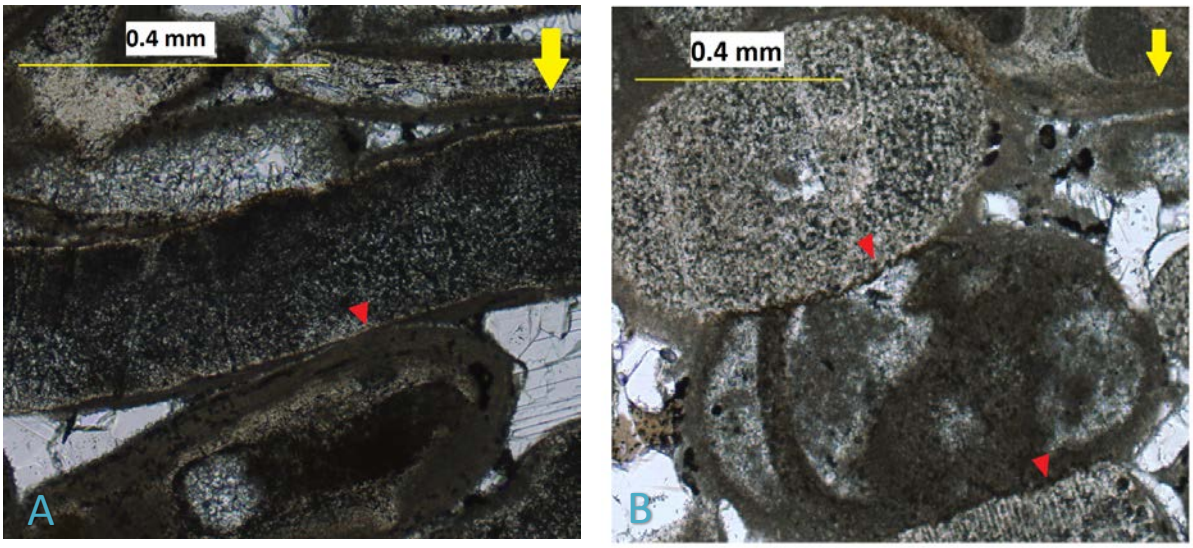

Figure 7: I1 and I2 type indentation features. (A) Thin section Indls3-8 in PPL with magnification 10x. Red arrow points to type I1 indentation of grains, caused by dissolution. Classification of I1 indicates there is little to no indentation occurring along the grain boundary. (B) Thin section IndLs5-3 in PPL with magnification 10x. Red arrows point to dissolution features. Indentation of grains can be seen along with suturing along the grain boundary. Indentations are I2-type, indicating there is significant indentation or suturing occurring at the grain boundary. The yellow arrow is parallel to σ_1 for both (A) and (B).

6. Results

6.1 Microcracks

Microcrack density was recorded as counts per mm and measured both perpendicular and parallel to σ_1 within each thin section. Differences between the undeformed sample and deformed samples can be seen (Figure 8). The microcrack density in the undeformed sample, both perpendicular and parallel to σ_1, is smaller than the density of all deformed thin sections. The difference between the undeformed sample and the deformed samples indicates that triaxial deformation experiments induced microcracking within the samples. Deformed samples also indicate microcracking preferentially occurred parallel to σ_1, compared to the undeformed sample which had no preferred microcrack orientation (Figure 9).

The sample with the greatest microcrack density of 2.12 counts per mm was 3-8, deformed with fluid that was no allowed to reach equilibrium with the rock at 75°C and 10 MPa. Sample 3-17, deformed under similar conditions except at 50 MPa, has a smaller density of 1.61 counts

of microcracking per mm. Decreasing microcrack density with increasing pressure is also seen with samples deformed with fluid allowed to reach equilibrium with the rock, although to a lesser degree. For sample 5-3 and 5-8, deformed at 75°C and at 10 and 50 MPa respectively, microcrack density is 1.60 and 1.41 counts per mm. However, these counts were taken parallel to σ_1. Microcrack density perpendicular to σ_1 show little to no change between samples deformed under different pressures. Microcrack density perpendicular to σ_1 is 0.99 and 0.69 counts per mm in samples 3-8 and 3-17, indicating a small decrease in microcrack density with increased pressure. In samples 5-3 and 5-8 microcrack density perpendicular to σ_1 is 0.94 and 0.88, indicating almost no difference in microcrack density with increased pressure.

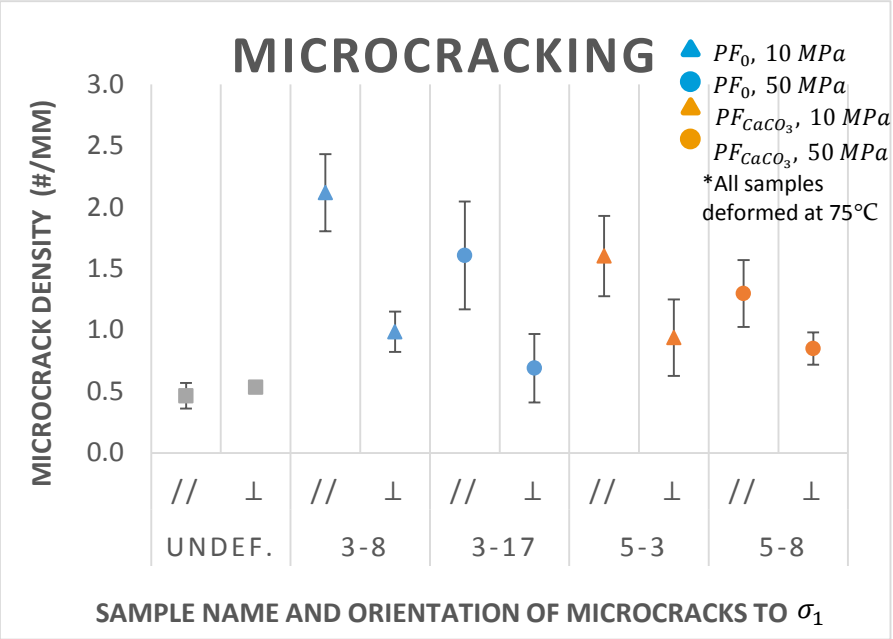

Figure 8: Microcrack density plotted by sample, and further divided by orientation of microcracks in reference to σ_1.

Samples deformed with different fluid conditions show variability in microcrack density. A difference of 0.52 counts per mm is seen between samples 3-8 and 5-3 parallel to σ_1. Between samples 3-17 and 5-8, deformed at higher pressure, this difference is halved to 0.2. In both cases microcrack density is greater in samples deformed with distilled water than samples deformed after fluid had reached equilibrium with the sample. Perpendicular to σ_1 these differences are almost non-existent.

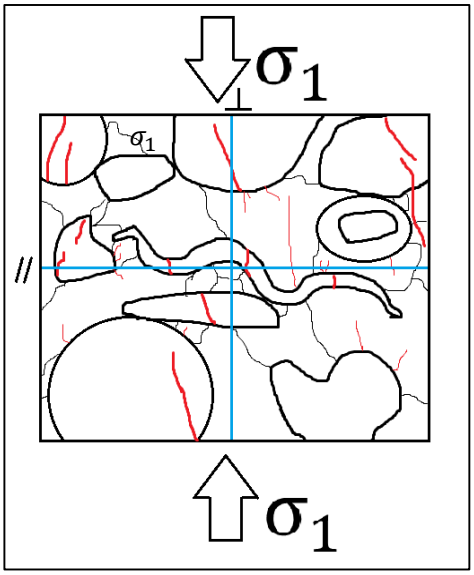

Figure 9: Illustration of propagation of microcracks (red) forming preferentially due to σ_1. Microcracks propagate parallel-subparallel to σ_1. This results in a greater number of microcracks crossing the parallel counting line, which is oriented perpendicular to σ_1.

6.2 Calcite Twins

Similar to microcrack density, the density of calcite grains exhibiting twins is greater in deformed samples compared to the undeformed sample (Figure 11). Twinned grain density is greater by up to 23x in the deformed samples, and at minimum roughly 1 magnitude greater.

Samples deformed under similar conditions but at different pressures show variability in twinned calcite grain density. Twinned grain density in sample 3-8 is 0.83 counts per mm both parallel and perpendicular to σ_1. Sample 3-17 was also deformed with distilled water, but at 50 MPa instead of 10 MPa. Twinned grain density in this sample is 0.98 parallel to σ_1 and 1.15 perpendicular to σ_1. This trend is similar in samples deformed with equilibrium fluid. Sample 5-3 has a twinned grain density of 0.49 counts per mm parallel to σ_1 and 0.54 counts per mm perpendicular to σ_1. In sample 5-8 twinned grain density is 0.78 and 1.06 counts per mm parallel and perpendicular to σ_1 respectively. Samples deformed at higher pressures have a greater twinned grain density than those at lower pressures, in samples deformed with both distilled water and equilibrium fluid. Samples deformed at higher pressures also show greater twinned grain density perpendicular to σ_1 compared parallel to σ_1 (Figure 14). However, at a lower pressure of 10 MPa this trend is not seen, and twinned calcite grain density is similar both perpendicular and parallel to σ_1 (Figure 10).

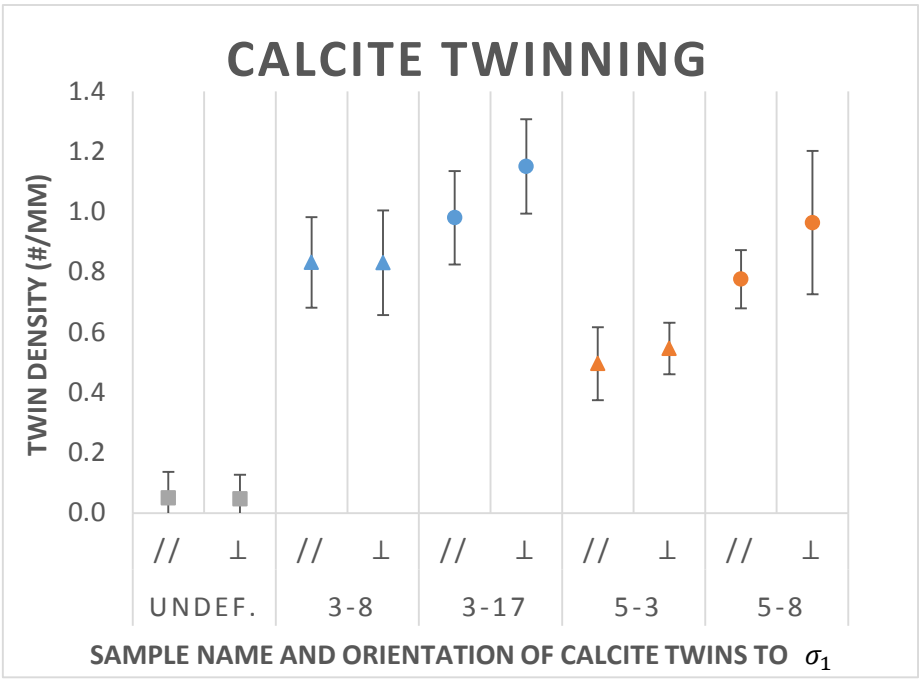

Figure 11: Calcite twin density plotted by sample, and further divided by occurrence along different oriented lines in reference to σ_1.

- PF_0, 10 MPa
- PF_0, 50 MPa
- PF_{CaCO_3}, 10 MPa
- PF_{CaCO_3}, 50 MPa

*All samples deformed at 75°C

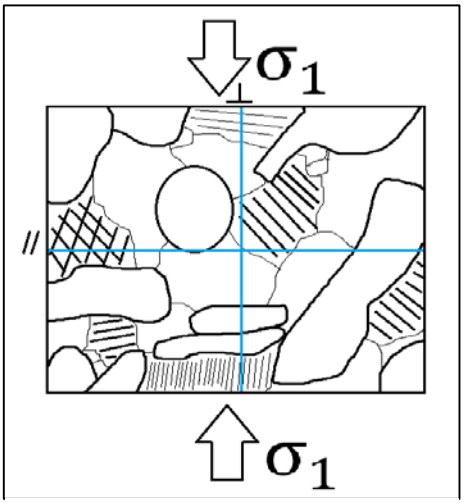

Figure 10: Illustration of calcite twinning within grains in low pressure deformation experiments. Calcite twin occurrence is equal both along the perpendicular and parallel blue lines.

Samples deformed with different fluid compositions show variation in twinned grain density. At low pressure, samples deformed with distilled water have a greater twinned grain density compared to samples deformed with equilibrium fluid. Samples deformed at higher pressure also have a greater twinned grain density in distilled water samples, but to a lesser degree. At higher pressure, a difference of only 0.09 counts per mm perpendicular to σ_1 exists between samples 3-17 and 5-8.

6.3 Indentations

Data from all deformed samples indicate indentations form preferentially perpendicular to σ_1 (Figure 13). Densities of indentation features parallel to σ_1 in the deformed samples are similar to the indentation density parallel to σ_1 in the undeformed sample (Figure 12). In the deformed samples, only samples saturated with distilled water show greatly increased indentation density perpendicular to σ_1 compared to the undeformed sample. Samples saturated with equilibrium fluid have only a small increase in indentation density perpendicular to σ_1 compared to the undeformed sample.

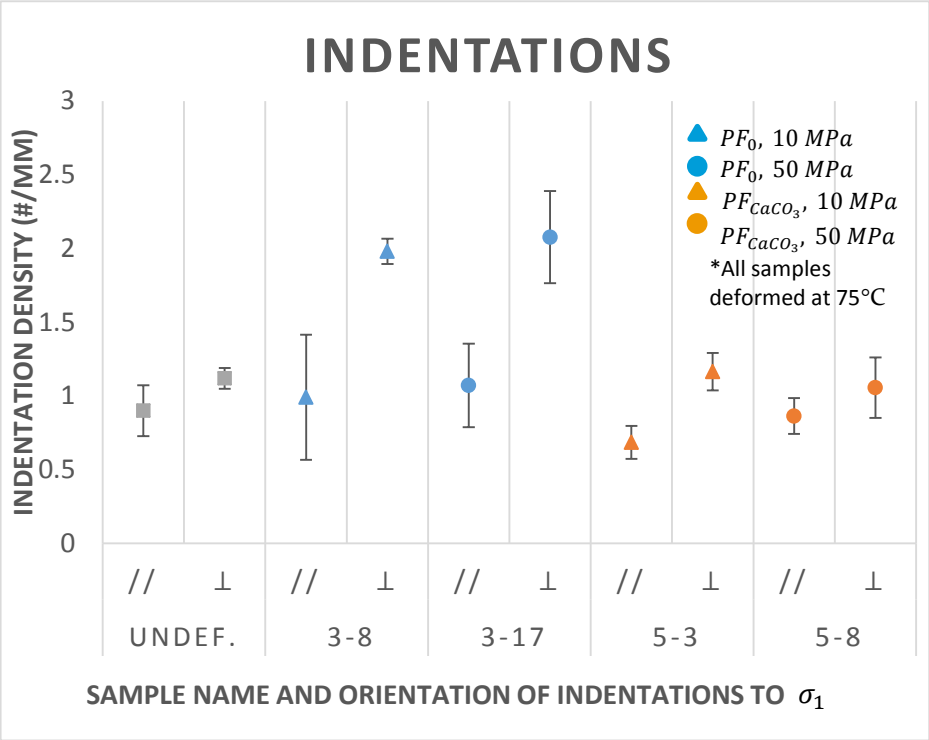

Figure 13: Indentation density plotted by sample, and further divided by occurrence along different oriented lines in reference to σ_1. Data includes both I1-type indentations and I2-type indentations.

There is almost no change in indentation density of samples deformed at different pressures. Samples 3-8 and 3-17 indicate a small increase in indentation density by 0.08 and 0.10 counts per mm parallel and perpendicular to σ_1 respectively. Samples 5-3 and 5-8 are indicate a small increase in indentation density by 0.18 counts per mm parallel to σ_1, however a decrease of 0.11 counts per mm perpendicular to σ_1.

Different fluid conditions in samples greatly affect indentation densities perpendicular to σ_1, and

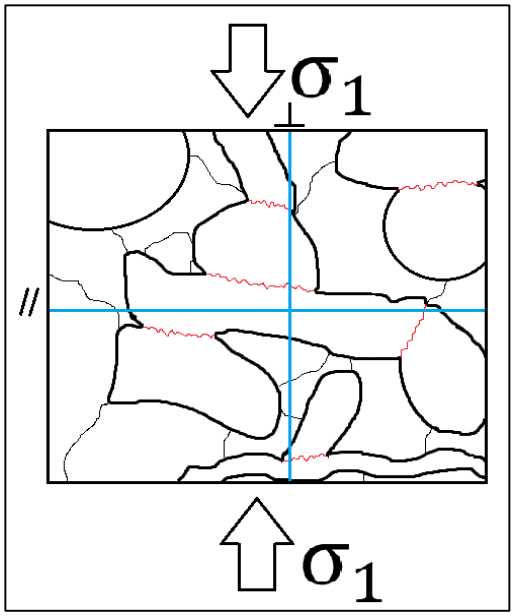

Figure 13: Illustration of indentations and grain-boundary suturing forming preferentially perpendicular to σ_1. This preferred alignment leads to a greater count density along the perpendicular line when compared to the parallel line.

only slightly affect indentation densities parallel to σ_1. The indentation density perpendicular to σ_1 in samples 3-8 and 3-17 is roughly 1.7x larger than the indentation density perpendicular to σ_1 in samples 5-3 and 5-8.

Indentation density is further divided by degree of indentation. Indentations in the deformed samples were primarily I2-type indentation, and so I2-type indentation data generally follows the trends seen in the total indentation data. At low pressures, I1-type indentation data parallel to σ_1 are very similar to data perpendicular to σ_1 (Figure 16). At high pressures, orientations of I1-type indentation are different parallel and perpendicular to σ_1(Figure 15).

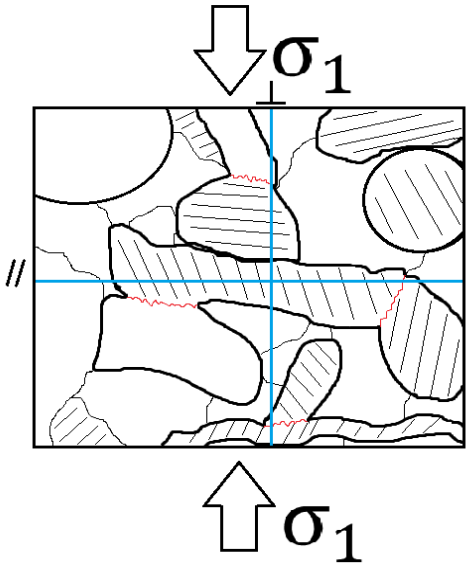

Figure 14: Schematic of possible explanation for a greater density of calcite twins along the perpendicular line at 50 MPa. With increased pressure and dissolution, damage to the crystallographic structure may occur at high-stress areas; high-stress will be felt at the grain of grains oriented parallel to σ_1. Damage may lower stress required to initiate calcite twinning, and so grains oriented along the perpendicular line are more likely to exhibit twinning.

7. Discussion

The data presented in this study indicate a clear difference between deformed and undeformed Indiana Limestone. Through deformation experiments samples developed a greater number of microcracks, calcite twins, and indentations. Microcracks and indentations both developed preferentially according to the direction of maximum principal stress, σ_1. Microcracks preferentially formed parallel to σ_1 in areas of high stress, causing lengthening perpendicular to σ_1 and shortening σ_1 as was expected (Figure 9). Indentations preferentially formed perpendicular to σ_1 at high-stress grain-grain boundary contacts, leading to dissolution at these sites (Figure 11).

The influence of fluid composition on the microstructures formed within these rocks is notable. Samples saturated with distilled water have a greater density of microcracks, calcite twins, and indentations compared to samples saturated with equilibrium fluid. According to Lizabeth and Zhu 2015, distilled water samples showed reduced strength compared to equilibrium fluid samples and also showed greater compaction due to dissolution and stress corrosion, which is in agreement with this study.

Sample 3-8, deformed with distilled water at 10 MPa, exhibited shear-enhanced compaction and then dilation during deformation experiments (Lisabeth and Zhu, 2015). The switch from shear-enhanced compaction to dilatancy can be caused by dislocation pile-up, which allows microcracking (Baud, 2000). However, no evidence of dislocation pile-up was seen in the photomicrographs. Sample 3-8 does exhibit a high density of dislocation calcite twins, enhanced due to calcite solubility, which most likely formed during shear-enhanced compaction. These twins are defects in the crystallographic structure, and can lower the stress

needed to initiate and propagate microcracks. Twinning may have occurred until the stress needed for microcracking was lower than the stress required to initiate mechanical twinning.

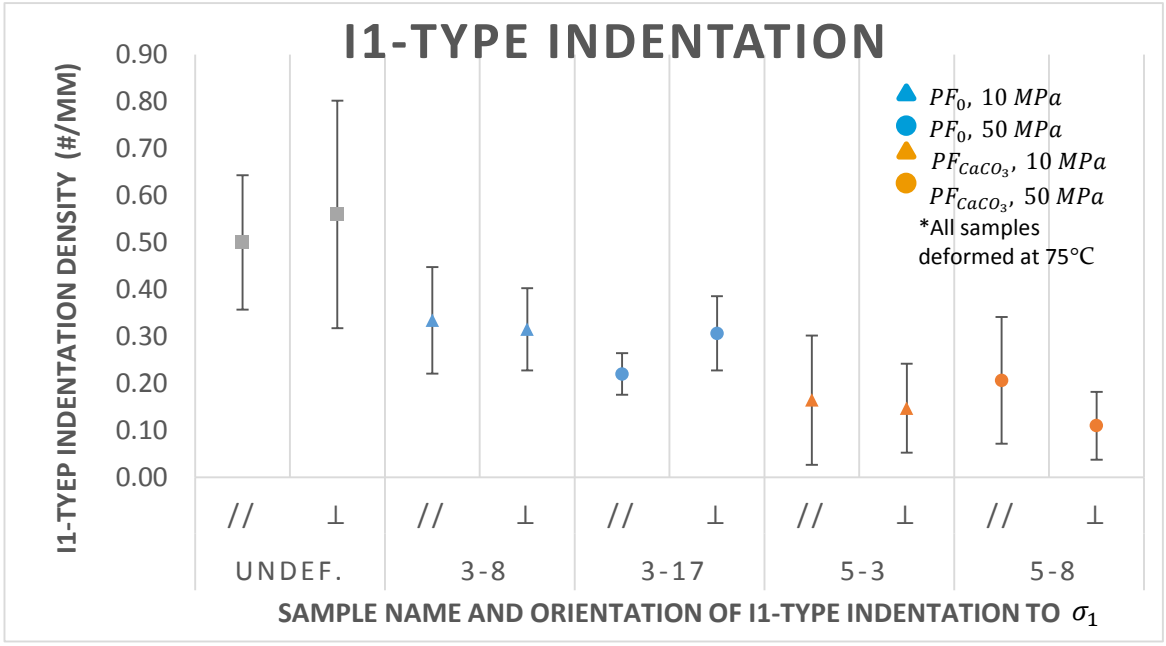

Figure 15: I1-type indentation density plotted by sample, and further divided by occurrence along different oriented lines in reference to σ_1.

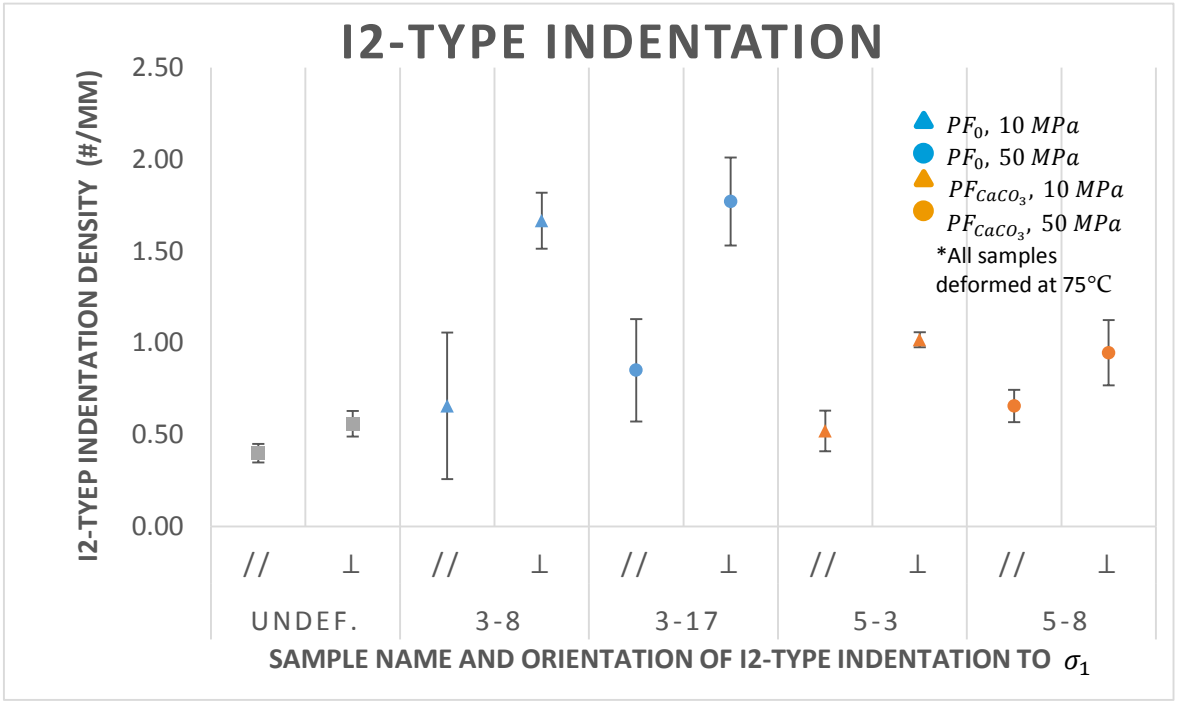

Figure 16: I2-type indentation density plotted by sample, and further divided by occurrence along different oriented lines in reference to σ_1.

Once this occurred, dilatancy began and microcracking took place. Sample 3-17 did not experience dilatancy during deformation, which may be reflected in the lower density of

microcracks (Lisabeth and Zhu, 2015). However, increasing pressure allowed for greater solubility and dissolution of calcite grains, which may have enhanced twinning while inhibiting microcracking. Sample 5-3, deformed with equilibrium fluid at 10 MPa, exhibited only dilatancy (Lisabeth and Zhu, 2015). Shear-enhanced compaction did not occur, and calcite twin density is lower in this sample than in sample 3-17. However, the microcrack density is also low compared to sample 3-8. Microcrack density may be lower because of the fluid used. Equilibrium fluid is not as corrosive as non-equilibrium fluid, and so less calcite twins form. Without these twins, the stress needed for microcracking may be larger than when twins are present. The difference between microcrack density in sample 3-17 and 5-3 may not be a direct causation of the fluid chemistry, but linked to the effect fluid chemistry has on calcite twin formation.

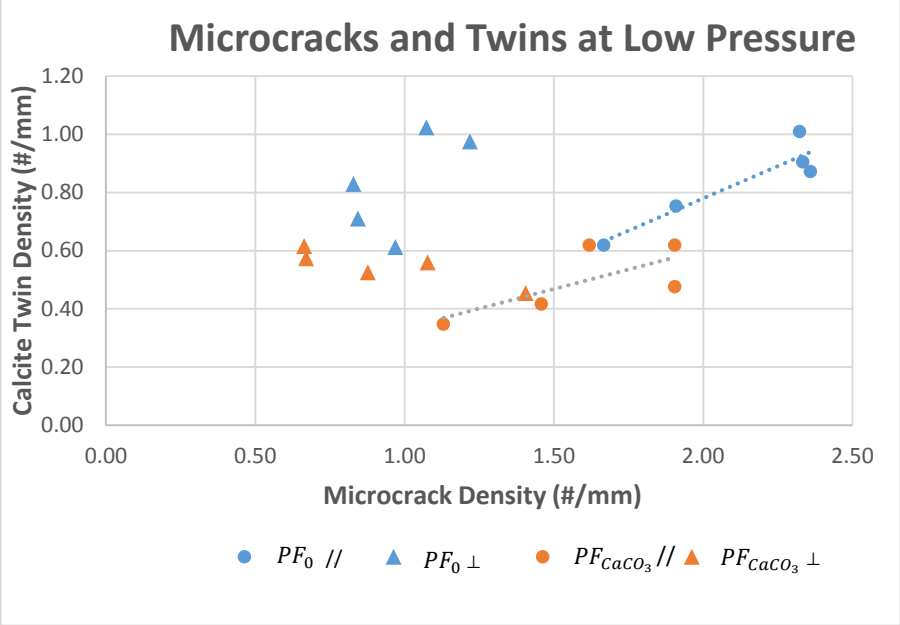

Figure 17: Comparison of microcrack density and calcite twin density at 10 MPa. Legend indicates differences in fluid composition and the orientation to σ_1. Each datum is a density for one line. Linear trends were added for two of the series to illustrate the coupling of microcracks and calcite twins.

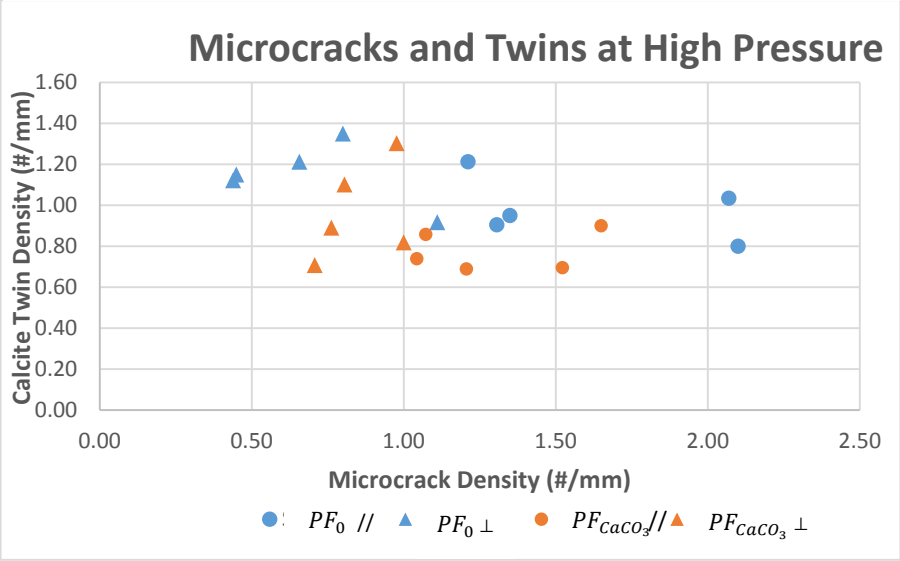

Figure 18: Comparison of microcrack density and calcite twin density at 50 MPa. Legend indicates differences in fluid composition and the orientation to $\boldsymbol{\sigma_1}$. Each datum is a density for one line. Notice there is no clear trend between microcracks and calcite twins.

Sample 5-8 experienced shear-enhanced compaction followed by grain crushing (Lisabeth and Zhu, 2015). The calcite twin density is high for this sample, while the microcrack density is slightly less than in sample 5-3. At high pressures, the corrosive power of the distilled water is enhanced and is able to initiate calcite twins in a greater number of grains. These twins may lower the stress needed for microcracks, however high pressure may increase the stress

needed for microcracking and inhibit microcracks. Thus, microcrack density is lower in samples deformed at higher pressures, even though twin density is higher. Increased pressure during deformation changes the deformation mechanisms occurring within the rock, from brittle to plastic deformation.

If calcite twins are indeed lowering the stress needed for microcrack formation at low pressure, coupling of calcite twins and microcracks should be seen. Evidence for the coupling of calcite twins and microcracks at low pressure is found in Figure 17. Microcrack density and calcite twin density parallel to σ_1 appear to follow a linear trend. However at high pressure and parallel to σ_1, microcrack density appears to be independent of calcite twin density (Figure 18). The data suggests that at low pressure microcrack formation is coupled with calcite twin formation, but at high pressure microcrack formation is not linked to calcite twin formation.

Indentation density does not appear to be strongly influenced by increasing pressure from 10 MPa to 50 MPa, despite the increased solubility of calcite at high pressure. A possible explanation could be the intensity of indentation is increasing, not the number of indentations along grain boundaries. Data comparing I1 type indentation density to I2 type indentation density does not support this possible explanation (Figures 15 & 16). Further division of the degree of indentation along grain boundaries may be needed to address this possibility.

At 50 MPa calcite twinning is greater perpendicular to σ_1 than parallel. The undeformed sample showed no preferential orientation of calcite twinning. Therefore, this preference was initiated during deformation experiments, but only at high pressure. Calcite twinning is a function of crystallographic structure, and therefore grain orientation. No preference in orientation was expected due to randomized grain orientation. This study is unable to definitively answer why calcite twinning is greater perpendicular to σ_1, however dissolution could play a role here. With increasing pressure, calcite solubility also increases allowing for greater amounts of dissolution. Dissolution will take place at areas of high stress, grain to grain boundaries, and may lead to imperfections in crystallographic structure. These imperfections may lower stress required to initiate dislocation, creating twinning. Since grains experiencing high stress will be aligned along the perpendicular line and parallel to σ_1, a greater number of twinning grains will be counted along this line (Figure 14).

8. Conclusion

In this study, I analyzed deformation microstructures of Indiana Limestone. I measured the linear density features of mechanical twins, microcracks, and grain boundary indentations, in order to obtain a better understanding of how fluid chemistry, temperature, and pressure affect deformation of limestones. Fluid chemistry has a clear influence on microstructures; distilled water samples had a higher density of microcracks, mechanical twins, and indentations when compared to equilibrium fluid saturated samples. Samples saturated with distilled water may experience enhanced solubility due to continuous dissolution, which promotes the formation of deformation microstructures. Pressure also has an effect on microstructures; at higher pressure microcrack density decreased and calcite twin density increased, transitions from brittle to plastic deformation. At low pressure, coupling between microcrack formation and calcite twin formation may occur with the presence of fluid. The effect of pressure on grain

boundary indentation does not show a clear trend. The interplay between microcracking, calcite twining, and pressure solution is complex, but important in understanding the way in which these rocks deform and fail. This study begins to address the deformation mechanisms that occur within these rocks, but is limited to a 2-D understanding of the structures. Increased qualitative analysis of microstructures should be considered, along with an expansion of the geometric measurements made on these microstructures.

Acknowledgements

I would like to thank my wonderful advisor Dr. Wen-lu Zhu for her support and patience throughout this long year. Our meetings always left me feeling determined and excited, and you always answered my questions in a way that was thorough and understandable. I would also like to thank Harry Lisabeth for always being available to answer questions, and for previously deforming the samples that I was gratefully able to work with. Lastly, I would like to thank the geology department as a whole. The wonderful professors and students I have met over the year have made this experience worth it, and are part of what makes studying geology so enjoyable. I hope our paths cross at an outcrop in the future.

References

Baud, P. (2000) Dilatancy, compaction, and failure mode in Solnhofen limestone. *Journal of Geophysical Research*, 105, B8, 19289-19393

Burkhard, M. (1993) Calcite twins, their geometry, appearance and significance as stress-strain markers and indicators of tectonic regime: a review. *Journal of Structural Geology*, 15(3), 351-368, doi:10.1016/0191-8141(93)90132-T

Cilona, A., Baud, P., Tondi, E., Agosta, F., Vinciguerra, S., Rustichelli, A., Spiers, C. (2012) Deformation bands in porous carbonate grainstones: Field and laboratory observations. *Journal of Structural Geology*, 45, 137-157

Doornhof, D., Kristiansen, T.G., Nagel, N.B., Pattillo, P.D., Sayers., C.M. (2006) Compaction and Subsidence. *Oilfield Review*, 18(3), 50-68

Ellsworth, W.L. (2013) Injection-Induced Earthquakes. *Science*. Vol. 341 no. 6142,1225942 , doi: 10.1126/science.1225942

Ferrill, D.A. (1991) Calcite twin widths and intensities as metamorphic indicators in natural low-temperature deformation of limestone. *Journal of Structural Geology*, 13(6), 667-675

Ferrill, D.A.; Morris, A.P.; Evans, M.A.; Burkhard, M.; Groshong, R.H., Jr.; and Onasch, C.M. (2004) Calcite twin morphology: a low-temperature deformation geothermometer. *Journal of Structural Geology*, 26, 1521-1529.

Lisabeth, H.P., Zhu, W. (2015) Effect of temperature and pore fluid on the strength of porous limestone. *American Geophysical Union*, doi: 10.1002/2015JB012152

Menendez, B., Zhu, W., Wong, T. (1996) Micromechanics of brittle faulting and cataclastic flow in Berea sandstone. *Journal of Structural Geology*. 18, 1-16. doi:10.1016/0191-8141(95)00076-P

Nagel, N.B. (2001) Compaction and subsidence issues within the petroleum industry: From Wilmington to Ekofisk and beyond. *Physics and Chemistry of the Earth Part A*, 26, 3-14, doi: 10.1016/S1464-1895(01)00015-1

Niemeijer, A.R., Spiers, C.J., Bos, B. (2002) Compaction creep of quartz sand at 400-600°C: experimental evidence for dissolution-controlled pressure solution. *Earth and Planetary Science Letters,*195, 261-275

Rutter, E.H. (1983) Pressure solution in nature, theory and experiment. *Journal of the geological society, London,* 140, 725-740 doi:10.1144/gsjgs.140.5.0725

Simmons, G., and Richter, D. (1976) Microcracks in rock: In the Physics and Chemistry of Minerals and Rocks: *New York: Wiley & Sons*, 105-137

Terzaghi, K. (1943) Theoretical Soil Mechanics: *New York: John Wiley & Sons*.

Vajdova, V., Baud, P., Wong, T. (2004) Compaction, dilatancy, and failure in porous carbonate rocks. *Journal of Geophysical Research: Solid Earth,* 109, B05204, doi: 10.1029/2003JB002508.

Vajdova, V., Zhu, W., Chen, T-M. N., Wong, T. (2010) Micromechanics of brittle faulting and cataclastic flow in Tavel limestone. *Journal of Structural Geology*, 32(8), 1158-1169, doi: 10.1016/j.jsg.2010.07.007

Wu, X., Baud, P., Wong, T. (2000) Micromechanics of compressive failure and spatial evolution of anisotropic damage in Darley Dale sandstone. *International Journal of Rock Mechanics and Mining Sciences*, 37, 143-160

Zhang, X., Spiers, C.J. (2005) Compaction of granular calcite by pressure solution at room temperature and effects of pore fluid chemistry. *International journal of rock mechanics and mining sciences*, 42, 950-960

Zhang, X., Spiers, C.J., Peach, C.J. (2011) Effects of pore fluid flow and chemistry on compaction creep of calcite by pressure solution at 150°C. *Geofluids,* 11, 08-122, doi: 10.1111/j.1468-8123.2010.00323.x

Appendix A: Data

Name	Orientation to sigma 1	Total avg. indentation density (per mm)	Indentation std. dev (σ)	Average I1 density (per mm)
IndLs3-8				
	Parallel	0.99	0.4247	0.33
	Perpendicular	1.98	0.0849	0.32
IndLs5-3				
	Parallel	0.68	0.1113	0.16
	Perpendicular	1.16	0.1276	0.15
Undeformed				
	Parallel	0.9	0.1732	0.50
	Perpendicular	1.12	0.0699	0.56
IndLs3-17				
	Parallel	1.072	0.2841	0.22
	Perpendicular	2.08	0.3125	0.31
IndLs5-8				
	Parallel	0.86	0.1218	0.21
	Perpendicular	1.06	0.2047	0.11

I1 standard deviation (σ)	Average I2 density (per mm)	I2 standard deviation (σ)	Average microcrack density (per mm)
0.1133	0.66	0.3988	2.12
0.0877	1.67	0.1532	0.99
0.1374	0.52	0.1110	1.60
0.0948	1.02	0.0410	0.94
0.1430	0.40	0.0500	0.47
0.2422	0.56	0.0699	0.54
0.0443	0.85	0.2790	1.61
0.0793	1.77	0.2388	0.69
0.1348	0.66	0.0880	1.30
0.0721	0.95	0.1778	0.85

Microcrack standard deviation (σ)	Average Twin density (per mm)	Twin standard deviation (σ)	Line name	Total Indentation density (per mm)
			PeR	0.45
0.3137	0.83	0.1501	**PeM**	1.05
			PeL	1.38
			PeRR	0.67
			PeLL	1.41
			PaD	1.90
0.1636	0.83	0.1736	**PaM**	1.91
			PaU	2.05
			PaUU	2.09
			PaDD	1.95
			PeR	0.71
0.3266	0.50	0.1214	**PeM**	0.62
			PeL	0.86
			PeRR	0.57
			PeLL	0.67
			PaD	1.24
0.3116	0.55	0.0856	**PaM**	1.14
			PaU	1.33
			PaUU	0.99
			PaDD	1.12
			PeR	0.80
0.1041	0.05	0.0866	**PeM**	1.10
			PeL	0.80
			PaD	1.12
0.0404	0.05	0.0807	**PaM**	1.19
			PaU	1.05
			PeR	0.95
0.4384	0.98	0.1548	**PeM**	0.90
			PeL	0.89
			PeRR	1.06
			PeLL	1.57
			PaD	1.85
0.2789	1.15	0.1569	**PaM**	2.30
			PaU	1.80
			PaUU	1.92
			PaDD	2.51
			PeR	0.87
0.2728	0.78	0.0967	**PeM**	1.04
			PeL	0.90
			PeRR	0.73
			PeLL	0.78
			PaD	1.02
0.1309	0.96	0.2377	**PaM**	1.41
			PaU	0.89
			PaUU	1.02
			PaDD	0.94

I1 density (per mm)	I2 density (per mm)	Microcrack density (per mm)	Twin density (per mm)	Total Indentation Incident (#)
0.25	0.20	2.32	1.01	9
0.52	0.52	2.33	0.90	22
0.29	1.10	1.67	0.62	29
0.26	0.41	2.36	0.87	13
0.35	1.06	1.91	0.75	28
0.29	1.61	1.07	1.02	39
0.44	1.47	0.84	0.71	43
0.34	1.71	0.83	0.83	42
0.20	1.89	0.97	0.61	41
0.29	1.66	1.22	0.98	40
0.00	0.71	1.90	0.48	15
0.14	0.48	1.90	0.62	13
0.38	0.48	1.62	0.62	18
0.13	0.43	1.13	0.35	13
0.17	0.50	1.46	0.42	16
0.19	1.05	0.67	0.57	26
0.13	1.01	0.88	0.53	26
0.28	1.04	0.66	0.62	28
0.04	0.95	1.40	0.45	24
0.09	1.03	1.08	0.56	26
0.35	0.45	0.50	0.00	16
0.70	0.40	0.35	0.15	22
0.45	0.35	0.55	0.00	16
0.49	0.63	0.56	0.14	16
0.63	0.56	0.49	0.00	17
0.56	0.49	0.56	0.00	15
0.20	0.75	2.10	0.80	19
0.25	0.65	1.35	0.95	18
0.25	0.64	2.07	1.03	18
0.15	0.90	1.31	0.90	21
0.25	1.31	1.21	1.21	31
0.24	1.61	0.44	1.12	38
0.40	1.90	0.45	1.15	46
0.25	1.55	0.80	1.35	36
0.25	1.67	0.66	1.21	38
0.39	2.13	1.11	0.92	52
0.35	0.52	1.04	0.74	20
0.30	0.74	1.52	0.70	24
0.25	0.65	1.65	0.90	18
0.09	0.64	1.07	0.86	17
0.04	0.73	1.21	0.69	18
0.09	0.93	0.98	1.30	22
0.18	1.23	1.00	0.82	31
0.04	0.85	0.76	0.89	21
0.04	0.97	0.81	1.10	24
0.19	0.75	0.71	0.71	20

I1 Incident (#)	I2 Incident (#)	Microcrack Incident (#)	Twin Incident (#)	Line Length (mm)
5	4	46	20	19.8
11	11	49	19	21
6	23	35	13	21
5	8	46	17	19.5
7	21	38	15	19.9
6	33	22	21	20.5
10	33	19	16	22.5
7	35	17	17	20.5
4	37	19	12	19.6
6	34	25	20	20.5
0	15	40	10	21
3	10	40	13	21
8	10	34	13	21
3	10	26	8	23
4	12	35	10	24
4	22	14	12	20.9
3	23	20	12	22.8
6	22	14	13	21.1
1	23	34	11	24.2
2	24	25	13	23.2
7	9	10	0	20
14	8	7	3	20
9	7	11	0	20
7	9	8	2	14.3
9	8	7	0	14.3
8	7	8	0	14.3
4	15	42	16	20
5	13	27	19	20
5	13	42	21	20.3
3	18	26	18	19.9
5	26	24	24	19.8
5	33	9	23	20.5
8	38	9	23	20
5	31	16	27	20
5	33	13	24	19.8
8	44	23	19	20.7
8	12	24	17	23
7	17	35	16	23
5	13	33	18	20
2	15	25	20	23.3
1	17	28	16	23.2
2	20	21	28	21.5
4	27	22	18	22
1	20	18	21	23.6
1	23	19	26	23.6
4	16	15	15	21.2

Appendix B: Photomicrographs

3-8	**3-8**	**3-8**
PaD	PaDD	PaUU
		

3-8	**3-8**	**3-8**
PaM	PaU	PeL
		

3-8	**3-8**	**3-8**
PeLL	PeM	PeR
		

3-8	**3-17**	**3-17**
PeRR	PaD	PaDD
		

3-17	**3-17**	**3-17**
PaM	PaU	PaUU
		

3-17	**3-17**	**3-17**
PeL	PeLL	PeM
		

3-17	3-17	5-3
PeR	PeRR	PaD
		

5-3	**5-3**	**5-3**
PaDD	PaM	PaU
		

5-3	**5-3**	**5-3**
PaUU	PeL	PeLL
		

5-3	**5-3**	**5-3**
PeM	PeR	PeRR
		

5-8	**5-8**	**5-8**
PaD	PaDD	PaM
		

5-3		
PaU	PaUU	PeL
		

5-8	**5-8**	**5-8**
PeLL	PeM	PeR
		

5-8	**Undeformed**	**Undeformed**
PeRR	PaD	PaM
		

Undeformed	**Undeformed**	**Undeformed**	**Undeformed**
PaU	PeL	PeM	PeR